ADVANCED MATERIALS
www.advmat.de

A Metal-Like Conductive Elastomer with a Hierarchical Wrinkled Structure

Seokmin Lee, Yongkwon Song, Yongmin Ko, Younji Ko, Jongkuk Ko, Cheong Hoon Kwon, June Huh, Sang-Woo Kim, Bongjun Yeom, and Jinhan Cho**

For the development of wearable electronics, the replacement of rigid, metallic components with fully elastomeric materials is crucial. However, current elastomeric electrodes suffer from low electrical conductivity and poor electrical stability. Herein, a metal-like conductive elastomer with exceptional electrical performance and stability is presented, which is used to fabricate fully elastomeric electronics. The key feature of this material is its wrinkled structure, which is induced by in situ cooperation of solvent swelling and densely packed nanoparticle assembly. Specifically, layer-by-layer assembly of metal nanoparticles and small-molecule linkers on elastomers generates the hierarchical wrinkled elastomer. The elastomer demonstrates remarkable electrical conductivity (170 000 and 11 000 S cm^{-1} at 0% and 100% strain, respectively), outperforming previously reported elastomeric electrodes based on nanomaterials. Furthermore, a fully elastomeric triboelectric nanogenerator based on wrinkled elastomeric electrode exhibits excellent electric power generation performance due to the compressible, large contact area of the wrinkled surface during periodic contact and separation.

The ultimate goal in portable, wearable, and attachable electronics is the complete replacement of rigid electrodes by elastomeric electrodes. Such elastomeric conductors must have metal-like electrical conductivity that is stable under repeated mechanical deformations, such as stretching, bending, and compression.[1–8] Several approaches have been attempted to achieve the desired electrical and mechanical performance, including serpentine or fractal-based layout design,[9,10] chemical reduction of a metal precursor,[11–13] and incorporation of conductive fillers with a high aspect ratio (i.e., metal nanowires (metal NWs) or carbon nanotubes (CNTs)).[14–17] However, to our knowledge, the elastomeric conductors based on nanomaterials reported to date have not exceeded an electrical conductivity of ≈10^5 S cm^{-1} (e.g., electrical conductivity of bulk gold and bulk iron ≈ 4.1×10^5 and 1.0×10^5 S cm^{-1}, respectively), despite the incorporation of a high loading amount of conductive nanomaterials into the elastomers.

The inadequately low conductivity of existing elastomeric conductor is due to the contact resistance between neighboring conductive components or the intrinsically low conductivity of the carbon-based materials used. Although the contact resistance can be lowered by thermal annealing and/or strong mechanical pressing, the application of such treatments is limited to conditions that do not damage the physical and/or chemical properties of the elastomers. Additionally, poor adhesion and phase separation between conductive components and elastomers induce serious adhesion failure under external mechanical stimuli, which significantly increases the resistance of the electrodes. Therefore, for use as electrodes under continuous external stimuli such as periodic contact/separation, adhesion between the conductive material and the elastomer should be carefully considered to ensure electrical stability.

A promising strategy for improving the electrical stability of elastomeric conductor is the control of their surface morphology. In particular, wrinkled elastomeric conductors may be a good alternative for realizing electrical stability under mechanical stimuli (particularly, periodic compressional and frictional stresses), because mechanical stresses are focused on the outermost regions of electrodes and because the valley regions in such electrode structures can minimize frictional stress. Generally, wrinkled elastomeric conductors have been prepared through metal deposition onto prestrained elastomers in uniaxial or biaxial direction.[18–21] However, these conductors cannot maintain high electrical conductivity under mechanical strain, experiencing cracking/disconnection of the continuous metallic thin layer as well as delamination between the metallic layer and the elastomeric substrate.[22–25] Additionally,

S. Lee, Y. Song, Dr. Y. Ko, Y. Ko, Dr. J. Ko, Dr. C. H. Kwon, Prof. J. Huh, Prof. J. Cho
Department of Chemical and Biological Engineering
Korea University
145 Anam-ro, Seongbuk-gu, Seoul 02841, Republic of Korea
E-mail: jinhan71@korea.ac.kr
Prof. S.-W. Kim
School of Advanced Materials Science and Engineering
Sungkyunkwan University
2066 Seobu-ro, Jangan-gu, Suwon 16419, Republic of Korea
Prof. B. Yeom
Department of Chemical Engineering
Hanyang University
222 Wangsimni-ro, Seongdong-gu, Seoul 04763, Republic of Korea
E-mail: byeom@hanyang.ac.kr
The ORCID identification number(s) for the author(s) of this article can be found under https://doi.org/10.1002/adma.201906460.

DOI: 10.1002/adma.201906460

prestrain and metal deposition processes pose much difficulty in preparing large-area wrinkled elastomeric electrodes. Although these electrodes can also be prepared through the transfer or deposition of conductive fillers such as metal NWs or CNTs onto prestrained elastomer films,[26,27] the abovementioned problems still represent major hurdles to fabricating elastomeric electrodes with high and stable electrical conductivity under various mechanical stimuli. Particularly, the previously reported processes are not suitable for the preparation of contact electrodes with arbitrary shapes such as curved structure, which limits their applicability. Thus, the challenge is to develop a method for fabricating wrinkled electrodes of a desired shape with high and stable electrical conductivity. Ideally, this would entail the stable adsorption of metal components onto elastomers by a simple solution process without requiring a prestrain step. Moreover, it would be desirable to minimize the contact resistance between neighboring metal components without additional treatments, such as thermal annealing or mechanical pressing.

The formation of closely packed Au nanoparticle (NP) arrays has a profound effect on the physical and electrical properties of Au NP-based films. For example, recent studies have reported that alkane thiol treatment of tetraoctylammonium bromide (TB)-stabilized Au NPs on inorganic nanotubes weakens the interfacial interaction between the Au NPs and inorganic surfaces, thereby increasing the mobility of Au NPs, which grow through Ostwald ripening.[28] It was also reported that neighboring Ag NPs with an interparticle separation of less than 5 Å can be fused, forming strong metallic bonds.[29] These reports suggest that consecutive ligand-exchange reactions between TB-Au NPs and small-molecule linkers can decrease the contact resistance between neighboring Au NPs, inducing metallic fusion, and generating densely packed Au NP arrays. Thus, we hypothesized that this ligand-exchange process could be adapted to overcome the aforementioned challenges with delamination and cracking, and achieve high electrical performance in wrinkled electrode structures.

Here, we report a wrinkled elastomer with bulk metal-like conductivity, high electrical stability, and a large electrode surface without the need for additional treatment processes by in situ cooperation of solvent swelling and metal NP assembly. For this study, poly(dimethylsiloxane) (PDMS) was used as a substrate for conductive elastomer because it has been widely used in the potential applications such as soft electronics and wearable devices taking advantages of stretchability. It can also allow a facile quantitative and qualitative comparison between our approach and previously reported processes. In our study, the elastomer demonstrated remarkable electrical conductivity (170 000 and 11 000 S cm^{-1} at 0% and 100% strain, respectively), which was close to metallic conduction. To further demonstrate the effectiveness and practicability of this elastomeric electrode, we fabricated a fully elastomeric triboelectric nanogenerator (TENGs) based on metal-like wrinkled elastomers, and investigated the possibility that they can generate higher electric output than those based on flat contact electrodes. Given our wrinkled elastomer's stable mechanical properties, large electrode area, and bulk metal-like electric conductivity, our approach may enable the design of a variety of flexible, stretchable, and compressible devices with high electrical performance.

The fabrication process is illustrated in **Figure 1**a. First, tetraoctylammonium bromide (TB)-stabilized Au NPs with a diameter of 7 ± 3 nm dispersed in toluene (Figure S1, Supporting Information) were layer-by-layer (LbL) assembled with tris(2-aminoethyl)amine (TA, $(NH_2CH_2CH_2)_3N$; molecular weight ($M_w \approx 146$) in ethanol onto a thiol (SH)-functionalized PDMS (shortly, PDMS) film (see Experimental Section, Supporting Information). In this ligand-exchange process, bulky TB ligands loosely bound to the surface of the Au NPs are first replaced by the SH groups of PDMS, and then by the NH_2 groups of the TA linkers. This exchange takes place because the primary amine group of TA has a higher affinity (by covalent bonding) for the surface of the Au NPs than the ammonium groups of the TB ligands. As shown in Fourier transform infrared (FTIR) spectra (Figure 1b and Figure S2, Supporting Information), the repeated deposition of TA onto the outermost TB-Au NP-coated substrate almost completely eliminated the TB ligands bound to the surface of the Au NPs (see the repeated generation and disappearance of the C—H stretching peaks at 2850–2950 cm^{-1}).

These FTIR results imply that vertically adjacent Au NPs within multilayers are connected by only one TA layer without bulky TB ligands. This close packing leads to partial metallic fusion among vertically adjacent NPs, as confirmed by field-emission scanning electron microscopy (FE-SEM). As shown in Figure 1c, the five-bilayered film exhibited a partially fused morphology with large grain boundaries instead of spherical Au NPs with a diameter of 7 ± 3 nm, which can be seen in the one-bilayer film. Therefore, our approach successfully minimizes the separation distance (and thus contact resistance) between neighboring Au NPs and leads to partial metallic fusion, without the need for any additional treatment (such as thermal annealing and/or mechanical pressing). These phenomena were more evidently observed when the amine-functionalized diethylenetriamine (DA, $M_w \approx 104$) with lower M_w than that of TA ($M_w \approx 146$) was used as an organic linker (Figure S3, Supporting Information). On the other hand, the use of bulky polymer linkers (i.e., poly(ethylene imine) (PEI)) with high M_w (≈50 000) effectively hindered metallic fusion between neighboring Au NPs (Figure S4, Supporting Information).

In order to calculate the separation distance between vertically adjacent Au NPs within the multilayers, we used atomistic molecular dynamics (MD) simulations of model systems for TA between Au layers (Figure 1d). When the ratio of the surface area occupied by adsorbed TA linkers to that occupied by adsorbed Au NPs (S_{TA}/S_{Au}) is approximately unity (Figure 1d(ii)) and therefore the Au NPs are covered by a TA monolayer adopting a flat conformation, the distance was estimated to be ≈5.6–5.7 Å. This minimized interparticle distance between neighboring Au NPs with low cohesive energy (3.81 eV per atom[30]) can facilitate reciprocal atom diffusion within the LbL-assembled Au NPs, which can have a positive effect on the enhancement of the electrical conductivity.

The surface topologies of $(TB\text{-}Au\ NP/TA)_n$-PDMS films ($n = 0.5$, 1, 1.5, and 2) were examined during each LbL deposition cycle from photographs and light diffraction patterns obtained from the reflection setup (**Figure 2**a and Figure S5, Supporting Information). The $(TB\text{-}Au\ NP/TA)_{0.5}$-PDMS film displayed a

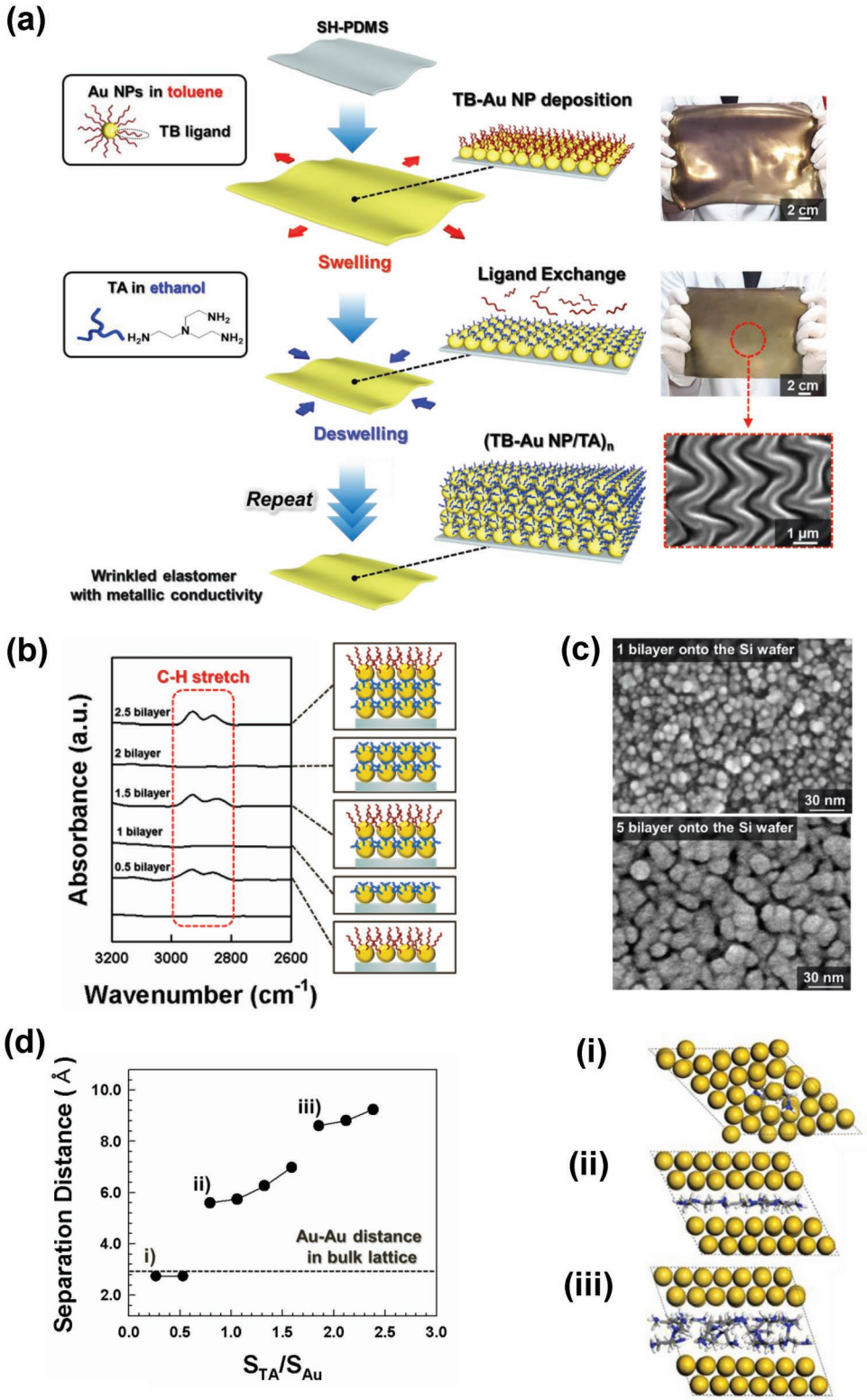

Figure 1. a) Schematic illustration of the fabrication process for wrinkled elastomeric electrodes using solvent swelling and contraction, and densely packed metal NP assembly. b) FTIR spectra and schematic representations of $(TB\text{-}Au\ NP/TA)_n$ multilayers. c) FE-SEM images of $(TB\text{-}Au\ NP/TA)_n$ ($n = 1$ and 5). d) MD-computed minimal distance between Au (100) surfaces separated by n TA molecules as a function of surface coverage, S_{TA}/S_{Au}, where S_{TA} and S_{Au} are the surface area covered by n TA molecules and the surface area of the Au layer, respectively. The gray dashed line represents the Au—Au distance in the bulk lattice (2.884 Å), implying that metallic fusion between initially separated Au slabs occurs. The images on the right side are the MD-simulated molecular structure of TA molecules between Au atomic surfaces at: (i) $S_{TA}/S_{Au} = 0.26$, (ii) $S_{TA}/S_{Au} = 0.79$, and (iii) $S_{TA}/S_{Au} = 1.85$.

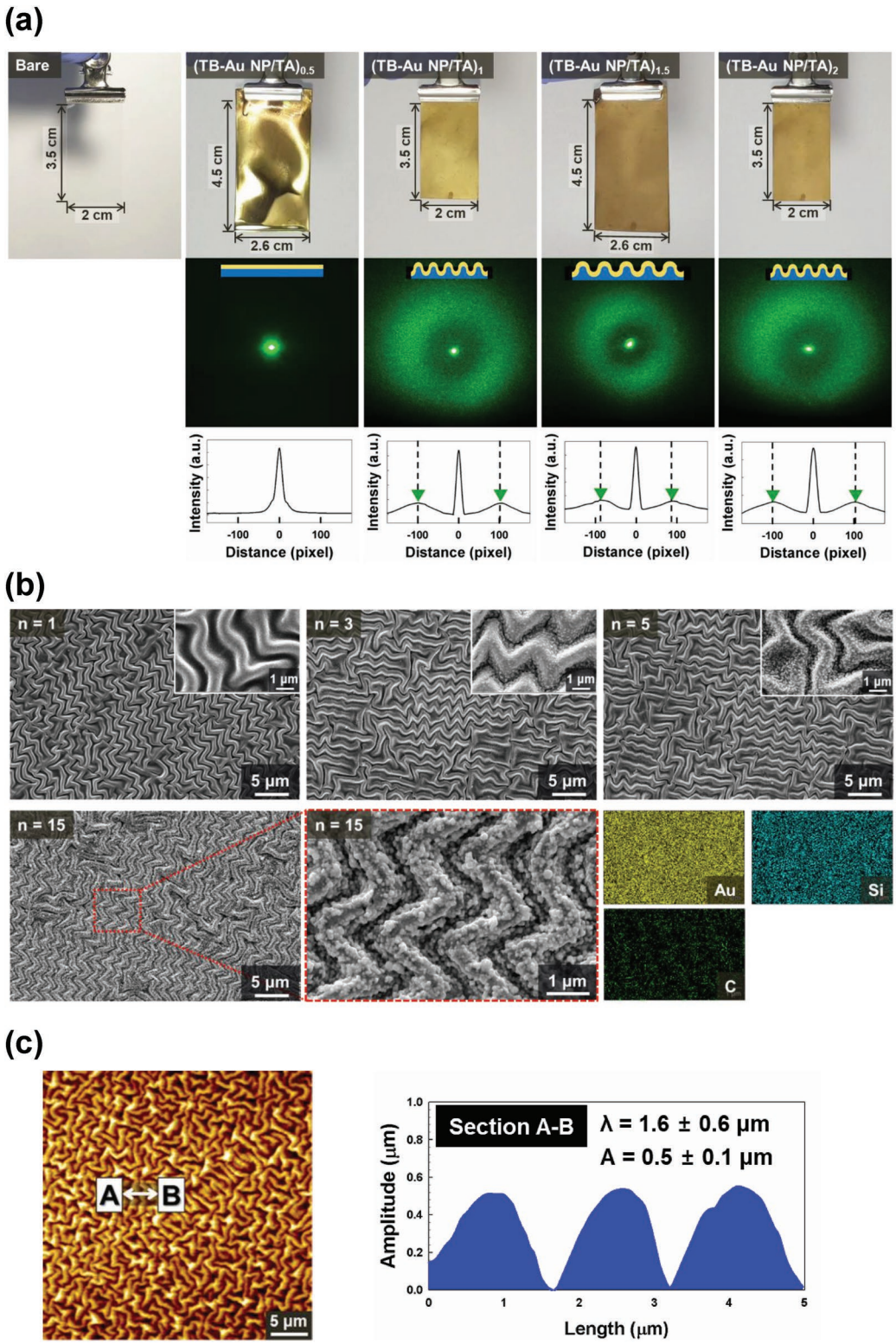

Figure 2. a) Photographic images and laser diffraction pattern images of wrinkled elastomeric electrodes during LbL deposition. The graphs show the intensity profiles of the diffraction ring pattern. The peaks of the intensity profile (green arrows) were narrower in the (TB-Au NP/TA)$_{1.5}$ sample than for samples with $n = 1$ or 2, implying a longer wrinkle wavelength. b) FE-SEM and EDX images of wrinkled elastomeric electrodes in the dried state after the deposition of (TB-Au NP/TA)$_n$ multilayers onto PDMS. EDX images shown on the bottom right side were obtained from (TB-Au NP/TA)$_{15}$. c) AFM image of a wrinkled elastomeric electrode (one-bilayer film) and its cross-sectional profile showing the wavelength and amplitude of the wrinkled structures.

metallic yellowish color and swollen state. The lateral size of the film increased up to ≈130% (i.e., 3.5 to 4.5 cm) relative to the initial length of the pristine PDMS film. In this case, the light diffraction pattern displayed a single central spot. These observations indicate that highly smooth and densely packed Au NP multilayers were formed on the swollen PDMS film, inducing strong reflection. When the swollen (TB-Au NP/TA)$_{0.5}$-PDMS film was dipped into the TA–ethanol solution for TA deposition, the swollen PDMS film returned to its initial film size due to the deswelling in ethanol. Simultaneously, the film undergoes a strong compressive force (particularly lateral compressive force). Considering that buckling instability starts when the interfacial stress exceeds a critical compressive force and is relieved,[31,32] we conclude that the wrinkled structure is formed by the contraction of the swollen PDMS.

After deswelling and ligand exchange deposition of TA, the surface of the (TB-Au NP/TA)$_1$-coated PDMS film exhibited a hazy and yellowish color owing to the formation of microwrinkles. The diffraction pattern displayed rings originating from the periodic formation of surface wrinkles in random orientations. This observation, together with that of film contraction described before, leads us to conclude that the packing density of the adsorbed TB-Au NPs is further increased upon TA deposition.

Although the deposition of the next TB-Au NP layer causes the film to reswell, the preadsorbed Au NP layers with high packing density effectively hindered the morphological change from a rough surface to a smooth surface. More specifically, when the TB-Au NPs were deposited onto the TA-coated substrate, the length of the film (i.e., (TB-Au NP/TA)$_{1.5}$-coated PDMS) again increased while maintaining a hazy appearance. In addition, the presence of the ring-shaped diffraction pattern and its decrease in diameter indicate that the surface wrinkles were expanded, maintaining random orientation. The swelling–contraction phenomenon repeated after further deposition of TA and TB-Au NPs. These results were also confirmed by reversible shifts in the peaks of the intensity profile (indicated by the green arrows) obtained from the diffraction patterns (Figure 2a).

To complement the results of the optical analysis above, we observed the surface morphologies of (TB-Au NP/TA)$_n$-coated PDMS in a dried state using FE-SEM and atomic force microscopy (AFM). As shown in Figure 2b, the deposition of (TB-Au NP/TA)$_n$ multilayers onto the 500-µm-thick PDMS films generated isotropically wrinkled surface patterns. In particular, these wrinkled structures were formed after deposition of the first bilayer of TB-Au NP/TA onto PDMS, which exactly coincided with the optical images shown in Figure 2a. In this case, the wavelength and amplitude of the formed surface wrinkling were measured (based on FE-SEM and AFM images) to be ≈1.6 ± 0.6 µm and 0.5 ± 0.1 µm, respectively (Figure 2b,c and Figure S6, Supporting Information). The wavelength was almost fixed after deposition of the first TB-Au NP layer despite the gradual increase in the (TB-Au NP/TA)$_n$ multilayer thickness (or the increase of bilayer number). However, when the thickness of PDMS was decreased up to 100 µm, the wavelength of the surface wrinkling was increased up to 3.4 ± 0.6 µm (amplitude ≈ 1.1 ± 0.1 µm) by the decreased compressive force (Figure S7, Supporting Information).

We also investigated the total thickness of (TB-Au NP/TA)$_n$ multilayer films adsorbed onto PDMS. Although the thickness of the one-bilayer films (i.e., (TB-Au NP/TA)$_1$) was ≈98 nm, the average bilayer thickness of the TB-Au NP/TA multilayers was ≈13 nm (Figure S8, Supporting Information). That is, when the PDMS substrate was dipped into the TB-Au NP–toluene solution for the formation of the first Au NP layer, the TB-Au NPs were densely packed onto the swollen PDMS films because there was no repulsion force among neighboring NPs. This is in contrast with conventional electrostatic LbL assembly of charged NPs in aqueous media, which generates a low packing density (<30%) in the lateral dimension owing to reciprocal electrostatic repulsion between NPs with the same charge.[33] Indeed, when anionic Au NP/cationic TA multilayers were deposited onto the substrate, the formed Au NP arrays exhibited low surface coverage without evident metallic fusion (Figure S9, Supporting Information). Also, the modulus of the (TB-Au NP/TA)$_1$ film on PDMS was calculated (Figure S10, Supporting Information).[34,35] The film exhibited a plane-strain modulus of ≈133 MPa which is much lower than that of a previously reported 100-nm-thick Au film (≈53 GPa) and a bulk Au thin film (82 GPa).[36] This result implies that the TB-Au NP-coated PDMS film can significantly lower the probability of mechanical failures, such as fracture or delamination of Au NP arrays on PDMS under external mechanical stimuli.[22–25] In addition, it was observed that the stretchability of the (TB-Au NP/TA)$_n$-coated PDMS in dried state was notably decreased compared to that of bare PDMS although the (TB-Au NP/TA)$_n$ multilayers induced the formation of wrinkled structure of PDMS substrate (Figure S11, Supporting Information). That is, the stretchability of Au NP multilayer-coated PDMS strongly depends on the mechanical property (i.e., the degree of stiffness) of the adsorbed Au NP multilayers.

Based on these results, we investigated the electrical conductivity and sheet resistance of the (TB-Au NP/TA)$_n$ multilayers on PDMS films. As the bilayer number (n) increased from 1 to 15, the electrical conductivity of (TB-Au NP/TA)$_n$ multilayers onto PDMS significantly increased from ≈0.02 (or total electrical conductivity including the thickness of PDMS substrate ≈3.9×10^{-6}) to 1.7×10^5 S cm^{-1} (total electrical conductivity ≈ 67 S cm^{-1}) and the sheet resistance decreased from ≈10^7 to 0.3 Ω sq^{-1} (**Figure 3**a). In particular, the (TB-Au NP/TA)$_{15}$-coated PDMS film exhibited typical metallic conduction behavior instead of the semiconducting behavior shown in electron hopping or tunneling conduction (Figure 3b and Figure S12, Supporting Information). That is, the resistivity of the (TB-Au NP/TA)$_{15}$ decreased linearly as the temperature decreased from 300 to 2 K, implying typical metallic conduction behavior. In this case, the multilayer-coated PDMS exhibited a positive temperature coefficient of 1.09×10^{-3} K^{-1}, as obtained from the equation $\Delta R_{(T)}/R_{(0)} = \alpha \Delta T$, where $R_{(T)}$ is the resistance at temperature T, $R_{(0)}$ is the resistance at T = 2 K, and α is the temperature coefficient. This value is characteristic of a bulk metal; for comparison, 3.71×10^{-3} K^{-1} is the temperature coefficient for bulk Au.

(TB-Au NP/TA)$_n$ (n = 5, 10, 15) multilayers exhibited highly stable electrical conductivity under external strain (Figure 3c,d, and Movie S1, Supporting Information). In particular, even after 100% stretching of the (TB-Au NP/TA)$_{15}$-coated PDMS film, its

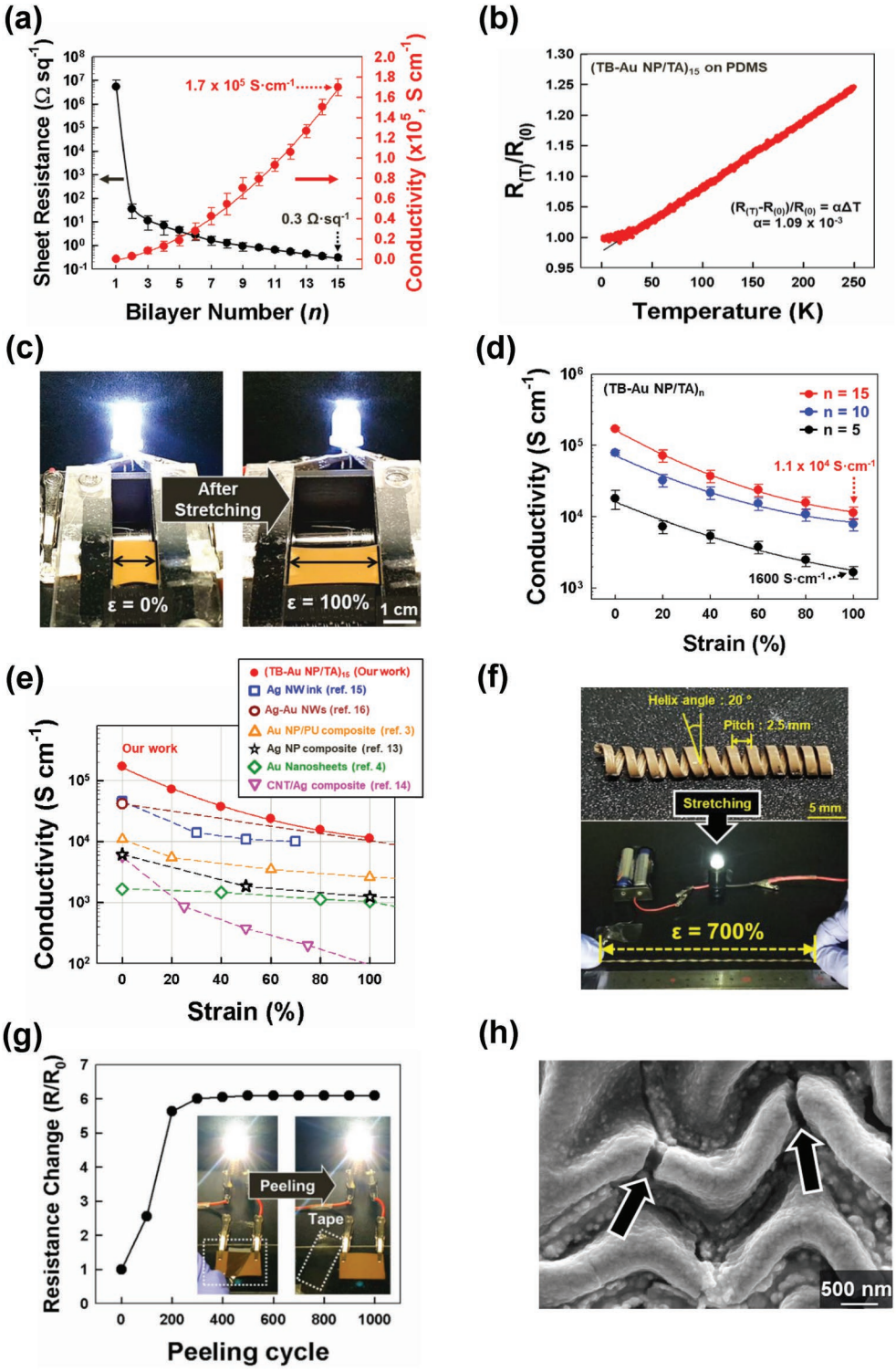

Figure 3. a) Sheet resistances and electrical conductivities of (TB-Au NP/TA)$_n$ multilayer-coated PDMS as a function of bilayer number (n). b) Resistance change ($R_{(T)}/R_{(0)}$) as a function of temperature (K) for (TB-Au NP/TA)$_{15}$ multilayer-coated PDMS. c) Photographs of (TB-Au NP/TA)$_n$-PDMS connected with LEDs before and after stretching. d) Electrical conductivity as a function of strain for the (TB-Au NP/TA)$_n$ multilayer-coated PDMS for different bilayer numbers. e) Performance comparison between (TB-Au NP/TA)$_{15}$-PDMS (our study) and previously reported elastomeric electrodes based on strain-dependent electrical conductivity. f) Photograph of a helical-structured (TB-Au NP/TA)$_{15}$-PDMS fiber with an LED connection before and after the application of 700% strain. g) Resistance change as a function of peeling cycle for (TB-Au NP/TA)$_{15}$-PDMS. The inset shows the photographs of the (TB-Au NP/TA)$_{15}$ multilayer-coated PDMS connected with LEDs before and after peeling tests using adhesive tape. h) FE-SEM image of (TB-Au NP/TA)$_{15}$-PDMS after 1000 peeling cycles.

electrical conductivity was ≈1.1×10^4 S cm^{-1} (Figure 3d), which was superior to previously reported materials (Figure 3e). We also confirmed that this electrical conductivity could be maintained during repetitive strain tests (at least 2000 cycles) (Figure S13, Supporting Information). Furthermore, we investigated the mechanical stability of (TB-Au NP/TA)$_{15}$ multilayer-coated PDMS under other types of mechanical deformation, namely, bending and normal compression. In the case of the bending test, the electrical resistance increased up to ≈110% of the initial resistance as the radius of curvature decreased from 16 to 2 mm (Figure S14a, Supporting Information); increasing the normal compression force from 0 to 200 N had no meaningful effect on the electrical resistance (Figure S14b, Supporting Information).

When we used helical-structured PDMS fibers (with a helix angle of 20° and a pitch of 2.5 mm) instead of 2D PDMS plates, the (TB-Au NP/TA)$_{15}$-PDMS fibers with a wrinkled surface could be stretched by ≈700%, accompanied by an increase in resistance from 0.7 to 6.5 Ω cm^{-1} (Figure 3f, Figure S15 and Movie S1, Supporting Information). Furthermore, our approach can also be applied to fabricate elastomeric conductors with various shapes, such as intaglio or embossed PDMS (Figure S16, Supporting Information). Particularly, the previously reported prestretching process has much difficulty in being directly applied to the large-area and/or curve-shaped elastomers (Figure S17, Supporting Information).

The hierarchically wrinkled surface morphologies of the (TB-Au NP/TA)$_n$ multilayer-coated PDMS films impart remarkable stability of electrical conductivity against external stimuli. We note that conductive (TB-Au NP/TA)$_n$ multilayers are deposited onto the entire surface, from the peaks to the valleys of the wrinkled PDMS patterns (see Figure S6b, Supporting Information). Generally, conventional conductive materials can be easily detached from PDMS substrates owing to their low affinity to PDMS; therefore, the wrinkled surfaces of PDMS—in addition to the stable covalent bonding between Au NPs and SH-PDMS, and between TA and Au NP—are highly advantageous for the maintenance of electrical conductivity under external mechanical stimuli. To demonstrate this, peeling tests using scotch tape were performed on (TB-Au NP/TA)$_{15}$-coated PDMS films. As shown in Figure 3g, Figure S18 and Movie S2 (Supporting Information), repetitive peeling increased the film resistance due to the partial crack of Au NP multilayers. However, after ≈230 cycles, no further resistance increase was observed because of (TB-Au NP/TA)$_{15}$ multilayers buried in the valley regions of the wrinkled PDMS, and because of the stable covalent bonding at the SH-PDMS/Au NP and Au NP/TA interfaces (Figure 3h). This clearly demonstrates that our elastomeric electrodes can maintain highly stable electrical conductivity under mechanical deformation. In addition to this stability arising from the wrinkled surface and the high affinity at the SH-PDMS/Au NP and Au NP/TA linker interfaces, we believe that this is also enhanced by partial metallic fusion among the neighboring Au NPs.

To further demonstrate the effectiveness and practicability of our elastomeric electrodes, we fabricated a fully elastomeric TENG based on metal-like wrinkled elastomers as a model system, which convert mechanical energy into electricity using the triboelectric effect coupled with electrostatic effects. Generally, charge generation and transfer in TENG devices are induced by periodic contact and separation between different triboelectric materials (Figure S19, Supporting Information).[37–44] As shown in **Figure 4**a, the resultant elastomeric TENG was composed of the wrinkled elastomeric contact electrode (i.e., (TB-Au NP/TA)$_{15}$-PDMS) with positive triboelectric polarity and a negative triboelectric PDMS film coated onto the top electrode. These two parts were separated with four PDMS pillars, leaving a narrow space. For quantitative performance comparison, we prepared TENG devices with rigid and flat Au electrodes (i.e., Au-sputtered Si wafers) (designated as flat TENGs). For the negative triboelectric PDMS plates, we prepared flat and embossed PDMS plates (Figure 4a and Figure S16, Supporting Information). Although it has been demonstrated the electric outputs of TENGs can be significantly improved by various strategies such as device structure, operation mode, fluorination treatment, and a kind of triboelectric materials,[37] our study focused on the difference of device performance between the elastomeric electrodes and the conventional metal electrodes.

Based on these triboelectric electrodes, we examined the change in electrical output of a flat and rigid electrode-based TENG (i.e., rigid contact electrode/flat PDMS-TENG) and elastomeric electrode-based TENGs (i.e., elastomeric electrode/flat PDMS-TENG and elastomeric electrode/embossed PDMS-TENG) as a function of repeated compressive force at an applied frequency of 5 Hz with 20% relative humidity. When the flat PDMS/rigid electrode-based TENGs were subjected to a pushing force of 30 N, the voltage and current output were ≈18 V and 2.0 μA cm^{-2}, respectively (Figure 4b, Figures S20 and S21, Supporting Information). As the compressive force was increased up to 90 N, these electrical outputs were also gradually increased up to ≈56 V and 3.4 μA cm^{-2}. However, in the case of elastomeric electrode/flat PDMS-based TENGs, as the compressive force increased from 30 to 90 N, their electrical outputs were significantly increased from 53 V and 4.2 μA cm^{-2} to 145 V and 8 μA cm^{-2}. Additionally, when the elastomeric contact electrode was combined with the embossed PDMS plate, the electrical output of the resultant TENG device was significantly increased up to ≈198 V and 17.2 μA cm^{-2} with stable electric output during 18 000 cycles (Figure 4b,c and Figure S22, Supporting Information), which outperformed those of TENG based on rigid contact electrode under same experimental conditions. The effect of the elastomeric electrode on the triboelectric potential of rigid electrode- and elastomeric electrode-based TENGs was further confirmed by analytical simulations using COMSOL software (Figure S23, Supporting Information).

Furthermore, resistors were connected as external loads to examine the effective power of the elastomeric electrode/embossed PDMS-TENG (Figure S24a, Supporting Information). With increasing load resistance, the instantaneous voltage peak was increased, whereas the current peak density was decreased owing to ohmic loss. Consequently, the instantaneous power output reached the maximum value (i.e., $W = I^2_{\text{peak}} R = 11$ W m^{-2}) at an external load resistance of ≈10 MΩ (Figure S24b, Supporting Information). Thus, the elastomeric electrode/embossed PDMS-TENG could be considered as a current source with a large internal resistance when the external resistance load was considerably smaller than the internal resistance. As a result, our approach using wrinkled elastomeric contact electrodes increases the contact area between compressible plates (i.e., these plates

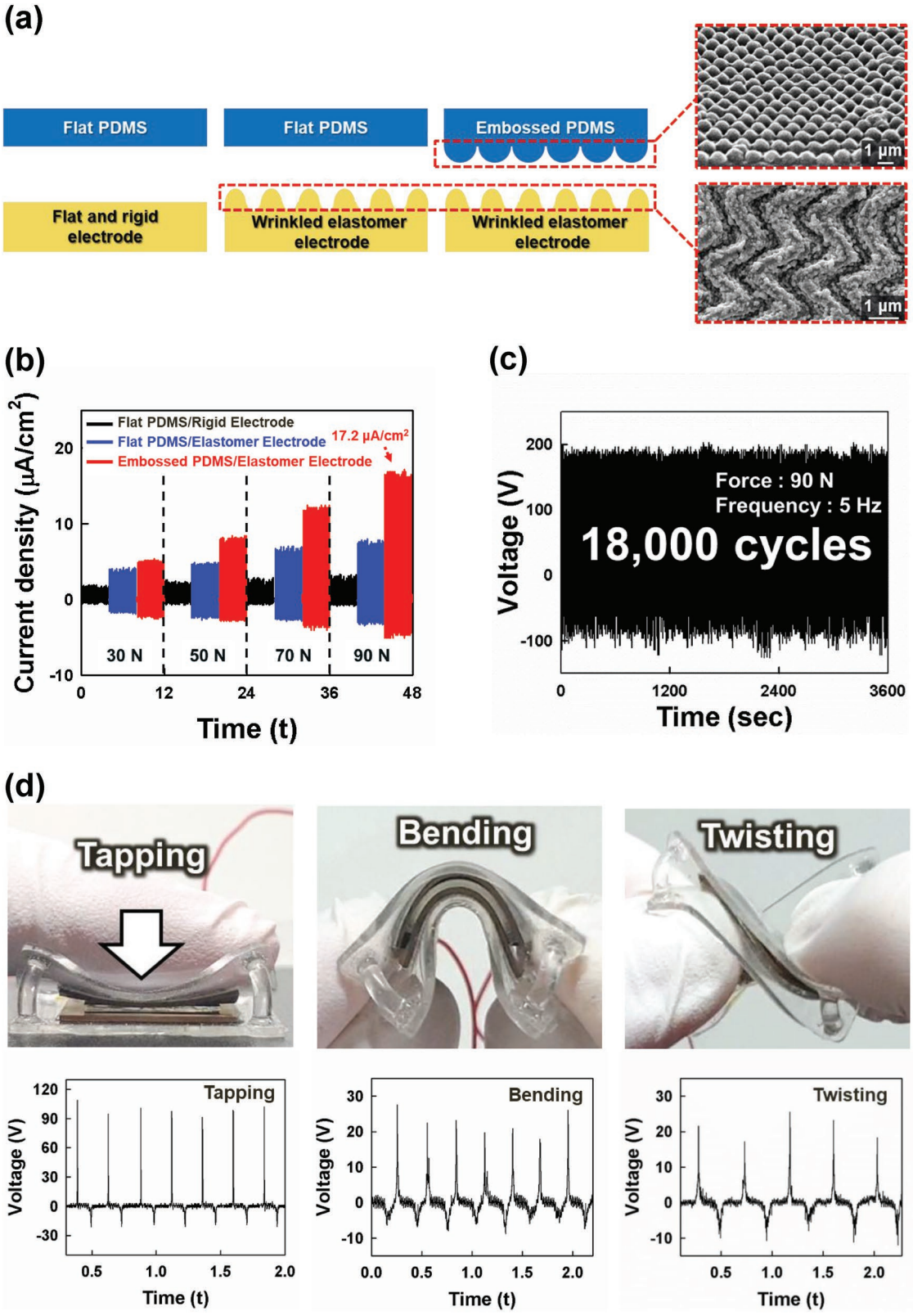

Figure 4. a) Schematic representation of TENG devices with three different kinds of electrode (i.e., flat PDMS/rigid, flat PDMS/wrinkled elastomeric, and embossed PDMS/wrinkled elastomeric). b) Current densities of the three TENG devices for different compressive forces. c) Stability test of the embossed PDMS/wrinkled elastomeric electrode-based TENG device under 18 000 cycles of 90 N compressive force. d) Photographs and output voltages of an all-elastomer-based TENG under tapping, bending, and twisting.

readily deform each other and fill vacant spaces, leading to a larger contact area), which notably increases the electric outputs of fully elastomeric electrode-based TENG. We also measured the performance of TENGs under various types of deformation caused by body movement, such as tapping, bending, and twisting (Movie S3, Supporting Information). Because our TENG was composed of only elastomers, it is freely deformable, and can generate power through repeated contact and separation between the elastomeric electrode and the embossed PDMS. Under finger tapping, bending, and twisting, the output voltage was ≈100, 25, and 20 V, respectively (Figure 4d, Figure S25 and Movie S4, Supporting Information). The stable power generation of the TENG under these deformations is because the elastomeric electrode can maintain high electrical conductivity under high strain and repeated contact and separation.

In summary, we demonstrated that wrinkled elastomeric conductors with highly stable metal-like conductivity can be easily prepared by the cooperation of solvent swelling and metal NP assembly. After the formation of densely packed TB-Au NP arrays on PDMS (i.e., SH-PDMS), the surfaces of the metal NP-coated PDMS were significantly wrinkled, showing a buckling wavelength and amplitude of ≈1.6 ± 0.6 μm and 0.5 ± 0.1 μm, respectively. These phenomena were caused by the strong lateral compressive force originating from contraction of the PDMS film during TA deposition in ethanol. When the (TB-Au NP/TA)$_{15}$-PDMS film was stretched from 0% to 100%, it maintained electrical conductivity from 1.7×10^5 to 1.1×10^4 S cm^{-1}. Additionally, these conductors exhibited highly stable electrical conductivity during repetitive bending, compressive, and peeling tests because of uniform and dense packing of Au NPs on the entire surface of the wrinkled PDMS, partial metallic fusion, and stable covalently bonded Au NP arrays. Furthermore, the electrical output of fully elastomeric TENG devices with contact electrodes (or electropositive electrodes) using our elastomeric conductors was significantly enhanced relative to TENG devices with flat and rigid electrodes as well as the previously reported elastomer-based TENGs. We believe that our approach can provide an important basis for developing and designing high-performance flexible and/or stretchable electronic devices composed of all-in-one elastomers.

Supporting Information

Supporting Information is available from the Wiley Online Library or from the author.

Acknowledgements

This work was supported by a National Research Foundation (NRF) grant funded by the Ministry of Science, ICT & Future Planning (MSIP) (2019R1A4A1027627, 2018R1A2A1A05019452, and 2016M3A7B4910619); as well as the Basic Science Research Program through the National Research Foundation of Korea (NRF) funded by the Ministry of Education (NRF-2017R1A6A3A04003192).

Conflict of Interest

The authors declare no conflict of interest.

Author Contributions

S.L., Y.S., Y.K., Y.K., J.K., C.H.K., J.H., S.-W.K., B.Y., and J.C. conceived the idea and designed the experiments. S.L. performed all the experiments. S.L., B.Y., and J.C. wrote and revised the manuscript. All authors discussed the results and commented on the manuscript.

Keywords

elastomeric electrodes, metal nanoparticles, multilayers, swelling, wrinkled structures

Received: October 2, 2019
Revised: November 14, 2019
Published online: December 12, 2019

[1] D.-H. Kim, J. A. Rogers, *Adv. Mater.* **2008**, *20*, 4887.
[2] J. A. Rogers, T. Someya, Y. Huang, *Science* **2010**, *327*, 1603.
[3] Y. Kim, J. Zhu, B. Yeom, M. Di Prima, X. Su, J.-G. Kim, S. J. Yoo, C. Uher, N. A. Kotov, *Nature* **2013**, *500*, 59.
[4] G. D. Moon, G.-H. Lim, J. H. Song, M. Shin, T. Yu, B. Lim, U. Jeong, *Adv. Mater.* **2013**, *25*, 2707.
[5] S. Yao, Y. Zhu, *Adv. Mater.* **2015**, *27*, 1480.
[6] Z. Bao, X. Chen, *Adv. Mater.* **2016**, *28*, 4177.
[7] C. Wang, C. Wang, Z. Huang, S. Xu, *Adv. Mater.* **2018**, *30*, 1801368.
[8] S. Choi, S. I. Han, D. Kim, T. Hyeon, D.-H. Kim, *Chem. Soc. Rev.* **2019**, *48*, 1566.
[9] J. A. Fan, W.-H. Yeo, Y. Su, Y. Hattori, W. Lee, S.-Y. Jung, Y. Zhang, Z. Liu, H. Cheng, L. Falgout, M. Bajema, T. Coleman, D. Gregoire, R. J. Larsen, Y. Huang, J. A. Rogers, *Nat. Commun.* **2014**, *5*, 3266.
[10] T. Pan, M. Pharr, Y. Ma, R. Ning, Z. Yan, R. Xu, X. Feng, Y. Huang, J. A. Rogers, *Adv. Funct. Mater.* **2017**, *27*, 1702589.
[11] D. C. Hyun, M. Park, C. Park, B. Kim, Y. Xia, J. H. Hur, J. M. Kim, J. J. Park, U. Jeong, *Adv. Mater.* **2011**, *23*, 2946.
[12] M. Park, J. Im, M. Shin, Y. Min, J. Park, H. Cho, S. Park, M.-B. Shim, S. Jeon, D.-Y. Chung, J. Bae, J. Park, U. Jeong, K. Kim, *Nat. Nanotechnol.* **2012**, *7*, 803.
[13] N. Matsuhisa, D. Inoue, P. Zalar, H. Jin, Y. Matsuba, A. Itoh, T. Yokota, D. Hashizume, T. Someya, *Nat. Mater.* **2017**, *16*, 834.
[14] K.-Y. Chun, Y. Oh, J. Rho, J.-H. Ahn, Y.-J. Kim, H. R. Choi, S. Baik, *Nat. Nanotechnol.* **2010**, *5*, 853.
[15] J. Liang, K. Tong, Q. Pei, *Adv. Mater.* **2016**, *28*, 5986.
[16] S. Choi, S. I. Han, D. Jung, H. J. Hwang, C. Lim, S. Bae, O. K. Park, C. M. Tschabrunn, M. Lee, S. Y. Bae, J. W. Yu, J. H. Ryu, S.-W. Lee, K. Park, P. M. Kang, W. B. Lee, R. Nezafat, T. Hyeon, D.-H. Kim, *Nat. Nanotechnol.* **2018**, *13*, 1048.
[17] D. Son, J. Kang, O. Vardoulis, Y. Kim, N. Matsuhisa, J. Y. Oh, J. W. F. To, J. Mun, T. Katsumata, Y. Liu, A. F. McGuire, M. Krason, F. Molina-Lopez, J. Ham, U. Kraft, Y. Lee, Y. Yun, J. B. H. Tok, Z. Bao, *Nat. Nanotechnol.* **2018**, *13*, 1057.
[18] H. Wu, Y. Huang, F. Xu, Y. Duan, Z. Yin, *Adv. Mater.* **2016**, *28*, 9881.
[19] S. Park, S. W. Heo, W. Lee, D. Inoue, Z. Jiang, K. Yu, H. Jinno, D. Hashizume, M. Sekino, T. Yokota, K. Fukuda, K. Tajima, T. Someya, *Nature* **2018**, *561*, 516.
[20] J. Tang, H. Guo, M. Zhao, J. Yang, D. Tsoukalas, B. Zhang, J. Liu, C. Xue, W. Zhang, *Sci. Rep.* **2015**, *5*, 16527.
[21] R. Nur, N. Matsuhisa, Z. Jiang, M. O. G. Nayeem, T. Yokota, T. Someya, *Nano Lett.* **2018**, *18*, 5610.
[22] O. Akogwu, D. Kwabi, A. Munhutu, T. Tong, W. O. Soboyejo, *J. Appl. Phys.* **2010**, *108*, 123509.

[23] Q. Wang, X. Zhao, *Sci. Rep.* **2015**, *5*, 8887.
[24] D. J. Lipomi, *Adv. Mater.* **2016**, *28*, 4180.
[25] T. Ibru, K. Kalaitzidou, J. K. Baldwin, A. Antoniou, *Soft Matter* **2017**, *13*, 4035.
[26] C. Yu, C. Masarapu, J. Rong, B. Wei, H. Jiang, *Adv. Mater.* **2009**, *21*, 4793.
[27] P. Lee, J. Lee, H. Lee, J. Yeo, S. Hong, K. H. Nam, D. Lee, S. S. Lee, S. H. Ko, *Adv. Mater.* **2012**, *24*, 3326.
[28] P. Ranjan, I. Kaplan-Ashiri, R. Popovitz-Biro, S. R. Cohen, L. Houben, R. Tenne, M. Lahav, M. E. van der Boom, *ACS Omega* **2018**, *3*, 6533.
[29] B. A. Korgel, S. Fullam, S. Connolly, D. Fitzmaurice, *J. Phys. Chem. B* **1998**, *102*, 8379.
[30] J. N. Israelachvili, *Intermolecular and Surface Forces*, Academic, San Diego, CA **2011**.
[31] N. Bowden, S. Brittain, A. G. Evans, J. W. Hutchinson, G. M. Whitesides, *Nature* **1998**, *393*, 146.
[32] S. Yang, K. Khare, P.-C. Lin, *Adv. Funct. Mater.* **2010**, *20*, 2550.
[33] J. Schmitt, G. Decher, W. J. Dressick, S. L. Brandow, R. E. Geer, R. Shashidhar, J. M. Calvert, *Adv. Mater.* **1997**, *9*, 61.
[34] H. G. Allen, *Analysis and Design of Structural Sandwich Panels*, Pergamon, New York **1969**.
[35] C. M. Stafford, C. Harrison, K. L. Beers, A. Karim, E. J. Amis, M. R. VanLandingham, H.-C. Kim, W. Volksen, R. D. Miller, E. E. Simonyi, *Nat. Mater.* **2004**, *3*, 545.
[36] H. D. Espinosa, B. C. Prorok, *J. Mater. Sci.* **2003**, *38*, 4125.
[37] C. Wu, A. C. Wang, W. Ding, H. Guo, Z. L. Wang, *Adv. Energy Mater.* **2019**, *9*, 1802906.
[38] K. Dong, X. Peng, Z. L. Wang, *Adv. Mater.* **2019**, 1902549.
[39] D. Liu, X. Yin, H. Guo, L. Zhou, X. Li, C. Zhang, J. Wang, Z. L. Wang, *Sci. Adv.* **2019**, *5*, eaav6437.
[40] X. Pu, M. Liu, X. Chen, J. Sun, C. Du, Y. Zhang, J. Zhai, W. Hu, Z. L. Wang, *Sci. Adv.* **2017**, *3*, e1700015.
[41] K. Parida, J. Xiong, X. Zhou, P. S. Lee, *Nano Energy* **2019**, *59*, 237.
[42] K. Y. Lee, J. Chun, J. H. Lee, K. N. Kim, N. R. Kang, J. Y. Kim, M. H. Kim, K. S. Shin, M. K. Gupta, J. M. Baik, S. W. Kim, *Adv. Mater.* **2014**, *26*, 5037.
[43] K. Parida, G. Thangavel, G. Cai, X. Zhou, S. Park, J. Xiong, P. S. Lee, *Nat. Commun.* **2019**, *10*, 2158.
[44] T. Liu, M. Liu, S. Dou, J. Sun, Z. Cong, C. Jiang, C. Du, X. Pu, W. Hu, Z. L. Wang, *ACS Nano* **2018**, *12*, 2818.

